

Topological defect lasers

This content has been downloaded from IOPscience. Please scroll down to see the full text.

2016 J. Opt. 18 014005

(<http://iopscience.iop.org/2040-8986/18/1/014005>)

View [the table of contents for this issue](#), or go to the [journal homepage](#) for more

Download details:

IP Address: 130.132.173.56

This content was downloaded on 12/12/2015 at 20:23

Please note that [terms and conditions apply](#).

Topological defect lasers

Sebastian Knitter¹, Seng Fatt Liew¹, Wen Xiong¹, Mikhael I Guy²,
Glenn S Solomon³ and Hui Cao¹

¹ Department of Applied Physics, Yale University, New Haven, CT 06520, USA

² Science & Research Software Core, Yale University, New Haven, CT 06520, USA

³ Joint Quantum Institute, NIST and University of Maryland, Gaithersburg, MD 20899, USA

E-mail: hui.cao@yale.edu

Received 6 August 2015, revised 28 September 2015

Accepted for publication 8 October 2015

Published 1 December 2015



CrossMark

Abstract

We introduce a topological defect to a regular photonic crystal defect cavity with anisotropic unit cell. Spatially localized resonances are formed and have high quality factor. Unlike the regular photonic crystal defect states, the localized resonances in the topological defect structures support powerflow vortices. Experimentally we realize lasing in the topological defect cavities with optical pumping. This work shows that the spatially inhomogeneous variation of the unit cell orientation adds another degree of freedom to the control of lasing modes, enabling the manipulation of the field pattern and energy flow landscape.

Keywords: topological defect, photonic crystal, optical vortex

(Some figures may appear in colour only in the online journal)

1. Introduction

Topological defects have been extensively studied in nematic liquid crystals and colloids [1–7]. There are various types of nematic defects that are characterized by a distinct orientational alignment of rod-shaped molecules or colloidal particles, creating a discontinuity in the director field around a fixed point. One important application of topological defects to photonics is the generation of optical beams with orbital angular momenta [6–8]. Also tightly focused laser beams have been used to manipulate topological defects in liquid crystals [8–10].

Previous studies focused on wavefront manipulation of transmitting optical beams via spatially dependent phase retardation. Due to the small size of liquid crystal molecules (~ 2 nm) and low refractive index modulation, light confinement at naturally occurring topological defects is negligible. Therefore these structures do not support optical resonances. We have shown recently [11] that by introducing a topological defect to a photonic crystal (PhC) optical resonances are created near the photonic bandedge [12–15]. However, these band-edge modes were spatially extended and light could easily escape through the boundaries [11].

In this paper we present an experimental realization of a topological defect cavity within a photonic crystal slab. By removing unit cells from the center of the topologically

perturbed PhC we attain strongly localized resonances [16]. These high quality factor (Q) modes exhibit power-flow vortices that can extend beyond the slab. Furthermore, we demonstrate lasing in the topological defect modes upon optical excitation of quantum dots (QDs) that are embedded in the structure. These results show that the topological defect provides a new degree of control over the characteristics of lasing modes.

2. Localized resonances with powerflow vortices

We consider a square lattice of ellipse-shaped air holes in a dielectric membrane. The air holes' dimensions as well as the lattice constant are on the order of the optical wavelength. The angular orientation of the elliptical holes varies spatially to produce a topological defect, as shown in figure 1(a). The angle between the major axis of an ellipse and the horizontal x -axis was set to $\phi = k\theta + c$, where θ denotes the polar angle of the center position of the ellipse, $k = 1$ is the topological charge, and c is set to $\pi/4$ [11]. For a hole-ellipticity of $\epsilon = 1.0$ the structure becomes a regular PhC and has no topological defect. A gradual increase of ϵ strengthens the topological defect. To enhance light confinement, 4×4 air holes were removed from the center of the topological defect

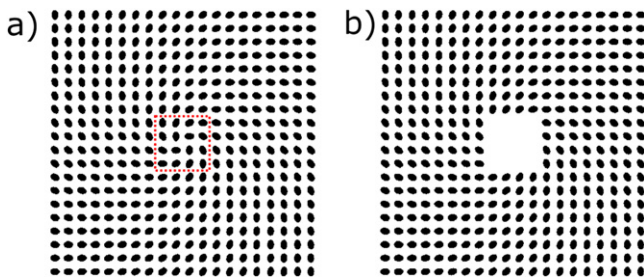


Figure 1. Introducing topological defect to a photonic crystal with anisotropic unit cell. (a) A square-lattice of air holes with elliptical cross-section embedded in a dielectric membrane. The major axis of each ellipse is rotated to an angle $\phi = k\theta + c$ from the x -axis. θ is the polar angle of the center position of the ellipse. $k = 1$ and $c = \pi/4$. Away from the center, the ellipses in each of the four quadrant are aligned in the same direction, forming crystalline domains that rotate 90° from one quadrant to the next. (b) Removing 4×4 air holes from the center of the topological defect structure to form a cavity.

structure (figure 1(b)), creating localized states in analogy to the PhC defect states [16].

We numerically calculated the localized resonances using the 3D finite-difference frequency-domain method [17]. Dimensions and material parameters were chosen to mimic a free-standing GaAs membrane in air: the refractive index of the membrane $n_{\text{slab}} = 3.5$, surrounding medium is air $n_{\text{vac}} = 1.0$, membrane thickness $d = 190$ nm, lattice constant $a = 220$ nm, filling fraction $f = 0.27$. The modes confined to the membrane are either TE (transverse-electric) polarized (with electric field parallel to the membrane) or TM (transverse-magnetic) polarized (with electric field perpendicular to the membrane). Since the TE modes experience stronger waveguiding inside the membrane and the gain medium (InAs QDs embedded in the membrane) provides stronger amplification for light in this polarization, the lasing modes are typically TE polarized [18]. Below we present the results for TE modes.

In the numerical simulation, we identify the high- Q modes. Figure 2(a) shows the calculated field profile for a defect mode of normalized frequency $a/\lambda = 0.23$, henceforth called mode (i). For comparison, we calculated the same mode in the regular PhC with circular holes ($\epsilon = 1.0$), as shown in figure 2(b). The mode profile remains nearly unchanged when the ellipticity of air holes is reduced from 1.4 to 1.0. However, the energy flow pattern changes significantly, as seen in the spatial map of the Poynting vector \vec{s} in figures 2(c) and (d). Each arrow points in the direction of local energy flux, and its size is proportional to the amplitude of the flux. For the regular photonic crystal defect state, the dominant energy flow points out of the central cavity (figure 2(d)). In the presence of the topological defect, the optical flux circulates clockwise (CW) within the cavity (figure 2(c)).

Figure 3(c) shows the calculated field profile for another defect mode at the normalized frequency $a/\lambda = 0.25$, henceforth called mode (ii). Unlike mode (i), mode (ii) shows a notable change in the field profile when the ellipticity of the

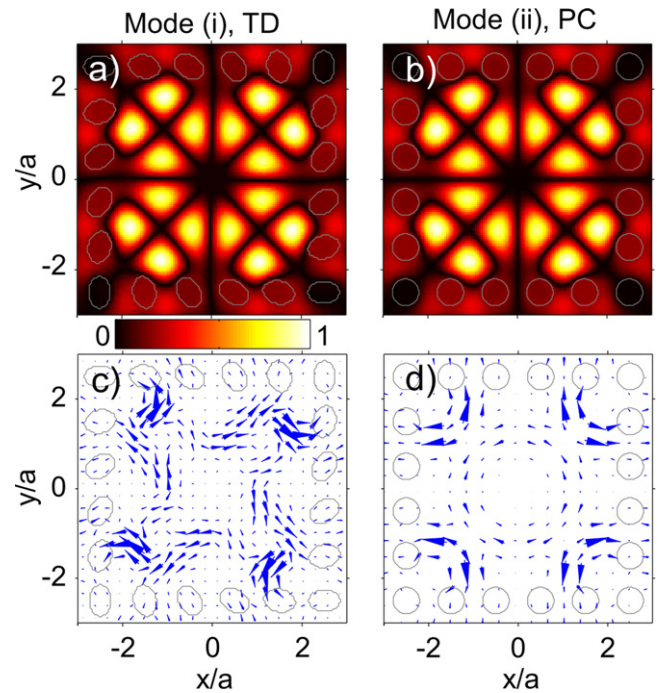


Figure 2. Numerical simulation of a localized resonance, mode (i), in the topological defect structure shown in figure 1(b), is presented in (a) and (c). For comparison, the mode in the structure with circular air holes is shown in (b) and (d). The modes are transverse-electric (TE) polarized, with the electric field parallel to the membrane ($x - y$ plane). The size of air hole array is 20×20 . The air holes surrounding the central defect region are outlined in gray. The spatial distribution of the magnetic field magnitude $|H_z|$ in (a) and (b) reveals little difference, but the spatial map of the Poynting vector (c) and (d) is significantly different for the two defect states. Each arrow points in the direction of local energy flux, and its size is proportional to the amplitude of the flux. While the energy flows out of the central region in (d), it circulates clockwise in (c).

air holes is changed between 1.0 and 1.4 (figure 3(a) and (c)). More specifically, the field pattern rotates CW when ϵ is increased from 1.0 to 1.4. The spatial map of the Poynting vector \vec{s} in figures 3(b) and (d) reveals an even more dramatic change in the energy flow. In the regular PhC defect state, the energy flows outward, mainly through the four corners of the central cavity. In contrast, a tightly confined CW circulating flux pattern arises at the center of a topological defect structure, indicating the formation of an optical vortex. The lateral dimension of the vortex is about one lattice constant (a), which is equal to a quarter of the vacuum wavelength ($\lambda/4$). Furthermore, the power-flow vortex of mode (ii) persists beyond the membrane. As seen in figures 3(e) and (f) the evanescent fields at distances of 405 nm and 905 nm above the top surface of the membrane possess circulating energy flows. These may transfer angular momentum to particles or molecules in the vicinity of the topological defect structure [19].

The drastic change in the energy flow is attributed to the spatial variation of the ellipse orientation in the topological defect structure. As seen in figure 1(a), the topological defect structure consists of four crystalline domains located in the four quadrants. The ellipses in each quadrant are aligned

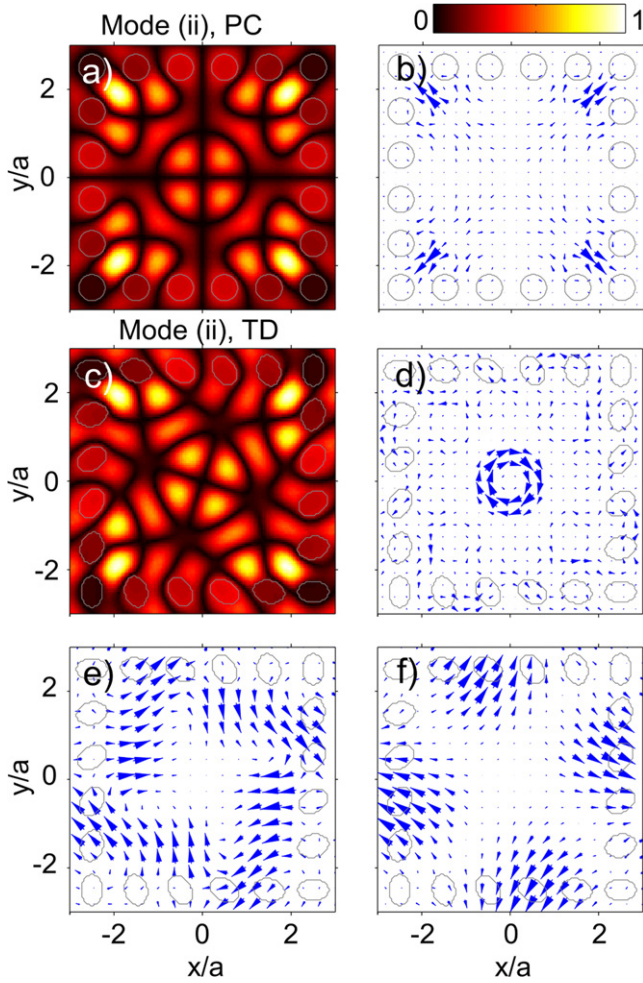


Figure 3. Numerical simulation of another localized resonance, mode (ii), in the same topological defect structure as in figure 2 is presented in (c) and (d). For comparison, the mode in the structure with circular air holes is shown in (a) and (b). The spatial distribution of the magnetic field magnitude $|H_z|$ in (a) and (c) reveals that the mode is rotated clockwise (CW) by the topological defect. The spatial map of the Poynting vector (b) and (d) illustrates the formation of an optical vortex in the topological defect structure. Panels (e) and (f) show the powerflow vortices of the evanescent fields of mode (ii) at distances 405 nm and 905 nm above the top surface of the membrane.

almost in the same direction, but they are rotated 90° from one quadrant to the next.

The rotation of the crystalline domains introduces chirality and breaks the balance in the out-coupling of CW and counter-clockwise (CCW) waves within the central cavity. This can be seen in figure 4(a), where the azimuthal component of the Poynting vector, $s_\theta = \vec{s} \cdot \vec{e}_\theta$, is plotted for mode (ii) in color scale, \vec{e}_θ is the unit vector in the azimuthal direction. Within the central cavity, the circulating flux is in the CW direction, $s_\theta < 0$; but outside the cavity the energy flow is dominated by CCW wave, $s_\theta > 0$. Because of the stronger coupling of CCW wave to the surrounding lattice, the wave left inside the cavity is predominantly CW [11].

The out-coupling can be tuned by varying the structural parameters. For example, we adjusted the filling fraction of air

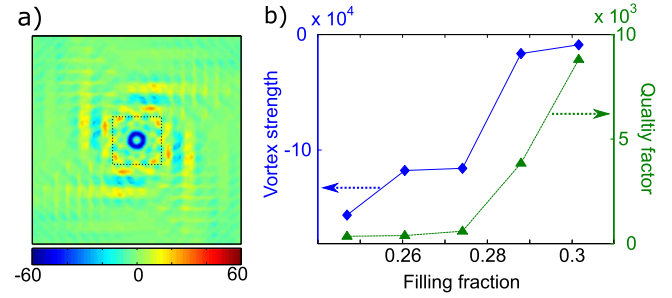


Figure 4. A trade-off between the vortex strength and the quality factor of the localized resonance in the topological defect structure. (a) The color map of the azimuthal component of the Poynting vector s_θ for mode (ii) in figure 3. In the lattice surrounding the central cavity (marked by black dotted square), the energy flow is dominated by the counter-clockwise (CCW) wave ($s_\theta > 0$), reflecting the stronger coupling of CCW wave out of the central cavity. (b) The Q -factor of mode (ii) increases with the filling fraction of air holes (green triangles), whereas the vortex strength (blue diamonds) decreases.

holes to change the strength of mode confinement within the central cavity. Figure 4(b) plots the vortex strength of mode (ii), defined as the spatially integrated azimuthal component of the Poynting vector, $\int s_\theta(r, \theta) r dr d\theta$, and the quality factor Q versus the filling fraction. As the filling fraction increases, the Q is increased, whereas the vortex strength is reduced. Since the residual photonic bandgap effect is stronger at the higher filling fraction, the confinement of mode (ii) is improved. Consequently, the imbalance between the CW and CCW wave components is reduced, and the powerflow vortex diminishes. Therefore, there is a trade-off between the optical vortex and the quality factor.

3. Lasing in topological defect cavity

The numerical study in the previous section shows that to obtain the optical vortex, the Q factor of the localized mode in the topological defect structure cannot be too high. This leads naturally to a question whether the Q is sufficient to support lasing.

In this section we experimentally demonstrate lasing of localized modes. We fabricated the topological defect structure in a semiconductor membrane, within an air filling-fraction range that supports optical vortices, and incorporated the gain medium. Once the samples were sufficiently pumped the high- Q modes started to lase and their spectral signature allowed us to identify the corresponding resonances in the passive system.

Figure 5 shows a fabricated topological defect structure. A 190 nm thick GaAs layer and a 1000 nm thick $\text{Al}_{0.75}\text{Ga}_{0.25}\text{As}$ layer were grown on a GaAs substrate by molecular beam epitaxy. Inside the GaAs layer, three uncoupled layers of InAs QDs, equally spaced by 25 nm GaAs barriers, were embedded to provide gain with optical excitation. The two-dimensional array of air holes was fabricated in the GaAs layer by electron-beam lithography and reactive ion etching (figure 5(a)). The $\text{Al}_{0.75}\text{Ga}_{0.25}\text{As}$ layer

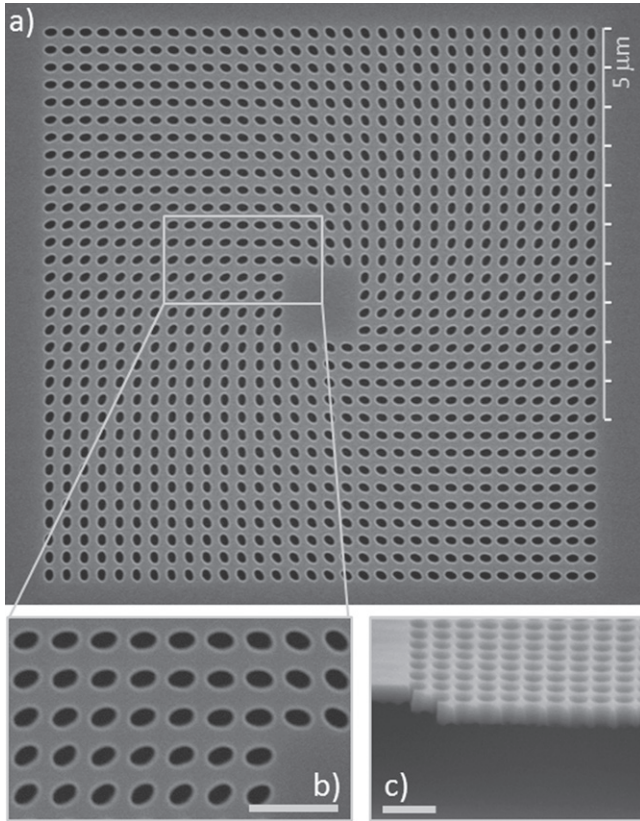


Figure 5. Scanning-electron microscope (SEM) images of a topological defect laser fabricated in a GaAs membrane. (a) Top-view SEM image of a square lattice of 32×32 air holes with elliptical shape. The ellipticity is $\epsilon = 1.4$. The lattice constant is $a = 220$ nm. The air filling fraction is 0.27. The major axis of each ellipse is rotated to an angle $\phi = \theta + \pi/4$, where θ is the polar angle of the center position of the ellipse. At the array center, 4×4 air holes are removed. (b) Magnified SEM of a section in (a), highlighted by the gray rectangle. (c) Tilt-view SEM image showing the free-standing GaAs-membrane. Scale-bars in (b) and (c) represent a length of 500 nm.

was then etched to leave a free-standing GaAs membrane in air (figure 5(c)). We fabricated many patterns of different structural parameters, e.g., the lattice constant a , the filling fraction, and the ellipticity ϵ (the ratio of the major axis over the minor axis of the ellipse) of air holes. By changing the lattice constant a , we were able to tune the wavelength of the defect-modes into the gain spectrum of InAs QDs to induce lasing action.

In the lasing experiments, the InAs QDs were optically excited by a mode-locked Ti:Sapphire laser (pulse duration ~ 200 fs, center wavelength ~ 790 nm, and pulse repetition rate ~ 76 MHz). The samples were mounted in a liquid Helium cryostat, and sample temperature was kept at $T = 10$ K to maximize the optical gain of InAs QDs. A long working distance objective lens ($50 \times$ magnification, 0.4 numerical aperture) was used to focus the pump light onto the sample at normal incidence. The emission, scattered out of the membrane, was collected by the same objective lens and

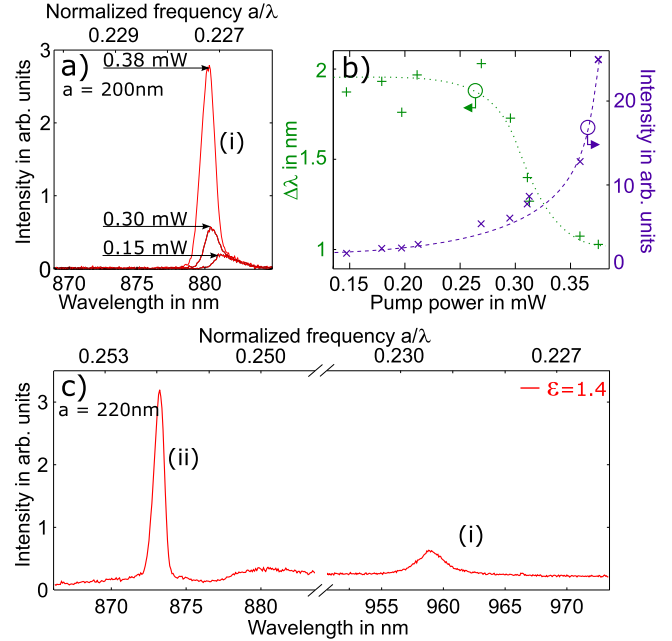


Figure 6. Experimental data of lasing in the topological defect cavity shown in figure 5. (a) Emission spectra of the $a = 200$ nm structure at the incident pump power of 0.15, 0.30, and 0.38 mW (from bottom to top). The emission peak is located at $\lambda = 880$ nm ($a/\lambda = 0.23$) and grows nonlinearly with pump power. (b) Spectrally-integrated intensity I and linewidth $\Delta\lambda$ of the emission peak in (a) as a function of the incident pump power P . The dotted–dashed curves guide the eye. When P exceeds 0.3 mW, I increases superlinearly and $\Delta\lambda$ drops abruptly, indicating the onset of lasing action. (c) Emission spectrum of the $a = 220$ nm structure. The emission peak shown in (a) is shifted to 960 nm (labeled (i)) and no longer lasing. A second emission peak exhibited lasing at $\lambda = 873$ nm ($a/\lambda = 0.25$).

directed to a grating spectrometer with a cooled charged device array detector (resolution ~ 0.3 nm).

Figures 6(a) and (b) present the experimental data for lasing in the topological defect structure with $a = 200$ nm and $\epsilon = 1.4$. The membrane thickness and filling fraction of air holes are identical to the values used in the numerical simulation (figures 2 and 3). However, the size of the air hole array is 32×32 , larger than the simulated one to increase confinement.

Figure 6(a) shows an emission peak at $\lambda = 880$ nm grows with pump power. Its relative frequency is $a/\lambda = 0.23$, corresponding to the mode (i) in figure 2. Its spectrally-integrated intensity, plotted as a function of the incident pump power P in figure 6(b), exhibits a threshold behavior. When P exceeds 0.3 mW, the peak intensity increases much more rapidly with pump power, meanwhile its linewidth decreases abruptly. This behavior indicates the onset of lasing action. The relatively broad linewidth of ~ 1 nm above the lasing threshold can be attributed to the hot carrier effect. Due to short pulse pumping, the density of electron-hole pairs varies in time, causing a change in the value of refractive index and a shift of lasing frequency [20, 21]. This transient frequency shift results in a broadening of the lasing line in the time-integrated measurement of the emission spectrum.

To tune the lasing frequency, we increased the lattice constant a to 220 nm while keeping the filling fraction of air holes unchanged. As shown in figure 6(c), the emission peak at 880 nm shifts to 960 nm, and the normalized frequency $a/\lambda = 0.23$ remained the same. Due to relatively weak gain at 960 nm, this mode (labeled (i) in figure 6(c)) no longer lased. Instead, another peak at $\lambda = 873$ nm started lasing (figure 6(c)), and its normalized frequency corresponds to mode (ii) in figure 3. From its normalized frequency $a/\lambda = 0.25$, we infer its wavelength in the previous structure with $a = 200$ nm to be $\lambda = 800$ nm, which falls outside the gain spectrum of InAs QDs. Hence, this mode did not lase previously. By tuning the structural parameters, we achieved lasing in different defect states.

4. Conclusion

By combining the topological defect with a PhC defect cavity, we demonstrate the formation of strongly confined optical resonances with high quality factors. Unlike the regular PhC defect states, the localized resonances in the topological defect structures support powerflow vortices. However, there is a trade-off between the vortex strength and the quality factor of the mode, which determines the lasing threshold. Experimentally we realized lasing in the topological defect cavities with optical pumping. Since the evanescent field beyond the structure possesses circulating energy flow, it may transfer angular momentum to particles or molecules in the proximity of the topological defect structure. Thus the optical vortex of the lasing mode may potentially be used for on-chip nanoparticle manipulation. Further experimental study is required to investigate the energy flows of different lasing modes and exploit the unique potential for applications in areas such as microfluidics for particle sorting and separation. More generally, this work shows that the spatially inhomogeneous variation of the unit cell orientation adds another degree of freedom to the control of a lasing mode, enabling the manipulation of its field pattern and energy flow landscape.

Acknowledgments

We thank Yaron Bromberg, Eric Dufresne and Chinedum Osuji for useful discussions. This work is supported by the MURI grant no. N00014-13-1-0649 from the US Office of Naval Research and by the NSF under the grant no. DMR-1205307.

References

- [1] Senyuk B, Liu Q, He S, Kamien R D, Kusner R B, Lubensky T C and Smalyukh I I 2013 *Nature* **493** 200
- [2] Muševič I 2013 *Phil. Trans. R. Soc. A* **371** 20120266
- [3] Loussert C, Delabre U and Brasselet E 2013 *Phys. Rev. Lett.* **111** 037802
- [4] Brasselet E and Loussert C 2011 *Opt. Lett.* **36** 719
- [5] Brasselet E 2010 *Phys. Rev. A* **82** 063836
- [6] Barboza R, Bortolozzo U, Assanto G, Vidal-Henriquez E, Clerc M G and Residori S 2012 *Phys. Rev. Lett.* **109** 143901
- [7] Barboza R, Bortolozzo U, Assanto G, Vidal-Henriquez E, Clerc M and Residori S 2013 *Phys. Rev. Lett.* **111** 093902
- [8] Brasselet E, Murazawa N, Misawa H and Juodkazis S 2009 *Phys. Rev. Lett.* **103** 103903
- [9] Smalyukh I I, Kaputa D S, Kachynski A V, Kuzmin A N and Prasad P N 2007 *Opt. Express* **15** 4359
- [10] Brasselet E, Murazawa N, Juodkazis S and Misawa H 2008 *Phys. Rev. E* **77** 041704
- [11] Liew S F, Knitter S, Xiong W and Cao H 2015 *Phys. Rev. A* **91** 023811
- [12] Soukoulis C M 2001 *Photonic Crystals and Light Localization in the 21st Century* vol 563 (Berlin: Springer)
- [13] Noda S and Baba T 2003 *Roadmap on Photonic Crystals* vol 1 (Berlin: Springer)
- [14] Sakoda K 2005 *Optical Properties of Photonic Crystals* vol 80 (Berlin: Springer)
- [15] Joannopoulos J D, Johnson S G, Winn J N and Meade R D 2011 *Photonic Crystals: Molding the Flow of Light* (Princeton, NJ: Princeton University Press)
- [16] Ryu H-Y, Kim S-H, Park H-G, Hwang J-K, Lee Y-H and Kim J-S 2002 *Appl. Phys. Lett.* **80** 3883
- [17] Comsol 2014 Multiphysics version 4.4
- [18] Cao H, Xu J, Xiang W, Ma Y, Chang S-H, Ho S and Solomon G 2000 *Appl. Phys. Lett.* **76** 3519
- [19] He H, Friese M E J, Heckenberg N R and Rubinsztein-Dunlop H 1995 *Phys. Rev. Lett.* **75** 826
- [20] Pompe G, Rappen T, Wehner M, Knop F and Wegener M 1995 *Phys. Status Solidi B* **188** 175
- [21] Jahnke F and Koch S W 1995 *Phys. Rev. A* **52** 17120